Acta Cryst B
STRUCTURAL SCIENCE
CRYSTAL ENGINEERING
MATERIALS
ISSN 2052-5206

Temperature-dependent crystal structure investigation of 4*f* hybridized thermoelectric clathrate $Ba_{8-x}Ce_xAu_ySi_{46-y}$

Jonas Sandemann, Hazel Reardon and Bo Brummerstedt Iversen*

Center for Integrated Materials Research, Department of Chemistry and iNANO, Aarhus University, Aarhus, DK-8000, Denmark. *Correspondence e-mail: bo@chem.au.dk

Received 19 October 2021
Accepted 9 December 2021

Edited by S. Grabowsky, University of Bern, Switzerland

Keywords: thermoelectrics; synchrotron powder diffraction; atomic displacement parameters; Debye and Einstein temperatures; clathrates.

Supporting information: this article has supporting information at journals.iucr.org/b

Thermoelectric materials allow for conversion of waste heat into electrical energy, and they represent a green solution for improving our energy efficiency. Inclusion of 4*f* electrons near the Fermi level may boost the Seebeck coefficient, which is essential for high thermoelectric performance. In this study, Ce was successfully substituted for Ba on the guest atom sites in the type-I clathrate $Ba_{8-x}Ce_xAu_ySi_{46-y}$ and the material was characterized using high-resolution synchrotron powder X-ray diffraction data measured from 100 K to 1000 K to investigate potential structural implications of the inclusion of a 4*f* element. The thermal expansion and bonding of the host structure are not affected by the presence of Ce, as seen from the linear coefficient of unit-cell thermal expansion of 7.30 (8) $\times 10^{-6}$ K^{-1} and the average host Debye temperature of 404 (7) K determined from the multi-temperature atomic displacement parameters, both of which are similar to values obtained for pure $Ba_8Au_ySi_{46-y}$. The anisotropic atomic displacement parameters on the guest atom site in the large clathrate cage populated by Ba surprisingly reveals isotropic behavior, which is different from all other clathrates reported in literature, and thus represents a unique host–guest bonding situation.

1. Introduction

As the world's energy consumption continues to increase, and the environmental impacts of fossil fuels is amplified, it is clearer than ever that we need to increase not only our capacity for green energy production, but also the efficiency with which we utilize energy. Thermoelectric materials can aid in this process through their ability to interconvert heat and electrical energy, which allow for harvesting of waste heat. The properties required for efficient thermoelectric energy conversion are reflected in the dimensionless figure of merit, $zT = S^2\sigma(\kappa^{-1})T$, where S is the Seebeck coefficient, σ the electrical conductivity, T the absolute temperature, and κ the thermal conductivity which has contributions both from the lattice (κ_l) and the charge carriers (κ_e). A high zT value means an efficient thermoelectric material, but maximizing this is not simple since S, σ and κ are not independent, but related through various materials characteristics such as the charge carrier concentration.

One approach to realizing high zT materials is finding structures that decouple σ and κ, such that high electrical and low thermal conductivity can be achieved simultaneously, a so-called phonon glass-electron crystal (PGEC) (Slack, 1995). Nolas *et al.* (1998) proposed Ge clathrates as potential thermoelectric materials due to their apparent PGEC nature, and since then clathrates have been intensely investigated (Christensen *et al.*, 2010). Clathrates are host–guest structures

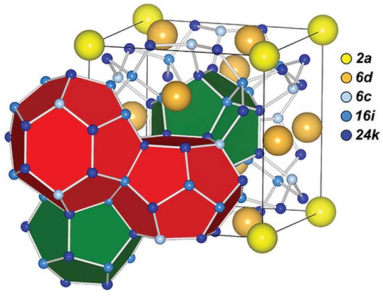

where the host atoms sit in a tetrahedral framework forming a network of face-sharing cages occupied by guest atoms. In the type-I clathrate structure, two different types of cages are present, a larger 24-atom tetrakaidecahedral and a smaller 20-atom dodecahedral cage. The structure can be viewed as a body centered arrangement of the dodecahedra within a 3D network of tetrakaidecahedral rods extending along the unit-cell axes, formed by joining the tetrakaidecahedra by their hexagonal faces. Type-I clathrates belong to cubic space group $Pm\bar{3}n$ and their general formula is G_8H_{46}, with G being guest atoms and H the host atoms. Fig. 1 shows the general clathrate structure along with a close-up of the two different host cages.

The host–guest structure is the reason clathrates can be considered as PGEC materials. Originally it was believed that the low κ observed in clathrates was due to tunneling of cations between different disordered sites inside the oversized cages similar to the properties of glasses (Sales *et al.*, 2001). This view was supported by the lack of crystalline peaks in the low-temperature κ_l of $Sr_8Ga_{16}Ge_{30}$ and $Eu_8Ga_{16}Ge_{30}$ but not in $Ba_8Ga_{16}Ge_{30}$, and coupled with the neutron diffraction observation of large off-center disorder of the Eu^{2+} and Sr^{2+} cations, but not of Ba^{2+} (Sales *et al.*, 2001). However, the cation tunneling mechanism could not explain why n-type $Ba_8Ga_{16}Ge_{30}$ had a crystalline peak in κ_l, while the peak was lacking in p-type $Ba_8Ga_{16}Ge_{30}$ (Bentien *et al.*, 2004, 2006). The two $Ba_8Ga_{16}Ge_{30}$ systems differ only slightly in Ga content and extensive single-crystal neutron and X-ray diffraction data showed that the structures and especially the behavior of the barium guest atoms are very similar (Christensen, Lock *et al.*, 2006). It was, however, recognized that the presence of loosely bonded cations in oversized clathrate cages resembles an independent (Einstein) oscillator with low-energy vibrational modes of energies similar to the acoustic modes of the host lattice (Sales *et al.*, 1999). Resonant scattering of phonons by the low-frequency guest atom 'rattling' modes was believed to disrupt phonon propagation through the lattice and causing low κ_l values (Sales *et al.*, 1999).The energies of the Einstein rattler modes can be estimated indirectly from analysis of multi-temperature atomic displacement parameters (ADPs) obtained from diffraction measurements or from modeling of heat capacity data (Bentien *et al.*, 2005). Direct evidence for the Einstein-like modes was given by Raman and inelastic neutron scattering data (Takasu *et al.*, 2006; Christensen, Juranyi & Iversen, 2006; Prokofiev *et al.*, 2013). However, the existence of independent Einstein vibrational modes somehow contradicts the notion that the vibrations interact with the host lattice modes, and the detailed mechanism needed further elaboration. This was achieved by measurement of the phonon dispersion of $Ba_8Ga_{16}Ge_{30}$ by single crystal inelastic neutron scattering, which revealed avoided crossing between the optical and acoustic branches in the phonon dispersion resulting in flattening of the acoustic branches and a lowering of κ_l (Christensen *et al.*, 2008). The guest rattling does not appear to have a profound effect on the electronic structure, as the electron mobility remains relatively high even when heat conduction is heavily suppressed (Cohn *et al.*, 1999). Lowering of the thermal conductivity with unaffected electrical conductivity is a signature of a PGEC material.

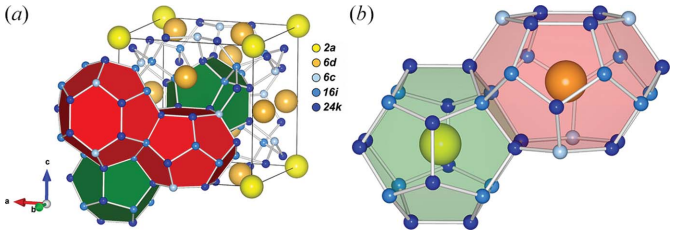

Figure 1
Visualization of the clathrate structure showing (*a*) the unit cell and (*b*) a closer look at the dodecahedral (green) and tetrakaidecahedral (red) cages. The atoms are colored according to their Wyckoff position.

The decoupling of σ and κ facilitates independent optimization of the thermoelectric power factor ($S^2\sigma$), which largely depends on the chemical bonding and the ensuing electronic band structure. The chemical bonding in clathrate structures can to a first approximation be understood in terms of the Zintl concept where a closed valence shell is achieved in the anionic covalent network through formal charge-transfer from the cation (Nesper, 2014; Shevelkov & Kovnir, 2010; Paschen *et al.*, 2003; Christensen *et al.*, 2010). In other words, the guest ions donate their valence electrons to the host atoms, which in turn form the tetrahedral covalent network that is the cage structure. This requires four electrons for every host atom and thus defines a guideline for understanding the stoichiometry of these compounds; with 46 host atoms per unit cell there are a total of 184 valence electrons required to form the tetrahedral bonding network of the host structure. This valence electron counting rule controls the stoichiometry when the constituent elements all have different valence. Detailed chemical bonding analysis using the quantum theory of atoms in molecules has shown that the simple Zintl model is actually a quite accurate description of the chemical bonding (Gatti *et al.*, 2003).

The incorporation of lanthanide guest atoms with 4*f* electrons has been envisioned as a way to engineer the electronic structure of clathrates (Bentien *et al.*, 2003). The idea was that the 4*f* electronic energy levels are placed close to the Fermi level, and this could give a peak in the density of state boosting the Seebeck coefficient. Prokofiev *et al.* (2013) showed that incorporation of Ce guest atoms in the clathrate cages led to an enhancement of the Seebeck coefficient by as much as 50% in comparison to a Ce-free reference with the same charge carrier concentration, and even at elevated temperatures. $Ba_8Au_xSi_{46-x}$ (BAS) was used as the model system for Ce incorporation due to its stability over a wide composition range of $4 \leq x \leq 6$ (Aydemir *et al.*, 2011; Zeiringer *et al.*, 2011).

The BAS system itself has been studied for thermoelectric applications, in part due to this large compositional range which encompasses both an electron-rich (n-type) and an electron-deficient (p-type) host structure. Assuming monovalent Au, the valence electron counting results in Zintl balance at an Au content of $x = 5.33$ predicting a transition from n- to p-type conduction as x crosses this value. Theore-

tical calculations corroborate the reduction in electron density at the Fermi level with substitution of Au in the Si host framework (Tse *et al.*, 2005). The transition from metallic-like to p-type semiconducting behavior has been confirmed at $x = 5.43$ using thermopower and Hall measurements (Aydemir *et al.*, 2011; Candolfi *et al.*, 2012). This dependence of the electronic properties on the composition has been exploited to make compositionally graded single crystals of BAS that can produce a voltage upon heating, even in the absence of a temperature gradient (Osakabe *et al.*, 2018; Yamasoto *et al.*, 2016). Stoichiometric control is not trivial in this system, however, and as-grown crystals often deviate from the nominal composition (Aydemir *et al.*, 2011; Candolfi *et al.*, 2012; Munetoh *et al.*, 2014; Saisho *et al.*, 2012; Jaussaud *et al.*, 2005). Au-rich impurities were observed at grain boundaries in arc-melted samples resulting in an Au-deficient clathrate phase compared to the nominal composition but subsequent annealing did prove effective in incorporating some of the Au from the impurities into the clathrate phase (Saisho *et al.*, 2012).

The study by Prokofiev *et al.* (2013) presented extensive transport properties, resulting in a rattling-enhanced Kondo interaction as the proposed mechanism underlying the enhancement of the thermopower caused by the presence of Ce on the guest sites. However, the structural analysis was somewhat crude and did not include the temperature dependence of the crystal structure. Since the specific nature of the host–guest chemical bonding determines the potential in which the guest atoms vibrate, it is clearly of interest to investigate whether the special 4*f*-hybridization leads to anomalies in the vibrational properties. Here we present a structural study of $Ba_{8-x}Ce_xAu_ySi_{46-y}$ (BCAS) using multi-temperature high-resolution synchrotron powder X-ray diffraction (PXRD) to further understand this unique material.

2. Experimental

2.1. Synthesis

A two-step arc melting procedure was used to synthesize the clathrate to achieve better control of the clathrate stoichiometry and potentially decrease impurities. Arc melting was conducted in a Compact Arc Melter MAM-1 from Edmund Bühler GmbH inside a glove box, allowing for the samples to be handled entirely under an argon atmosphere in order to prevent formation of oxide impurities. In the first step $BaSi_2$ and $CeSi_2$ were prepared by arc melting stoichiometric amounts of pure elements (Si: 99.999+ % metals basis, Alfa Aesar, Ba: >99% trace metals basis, Sigma Aldrich, Ce: 99.9% trace rare earth metals basis, Sigma Aldrich) under argon atmosphere, capturing the more volatile Ba and Ce in these stable silicides. Then, in the second step, these were mixed with Si and Au (99.9%) according to the nominal composition $Ba_6Ce_2Au_6Si_{40}$, and arc-melted to yield the final product. In both cases the chamber was under argon atmosphere and the sample was flipped and arc-melted multiple times to ensure complete reaction and a homogeneous product. The resulting ingot was then manually ground to a fine powder using an agate mortar and pestle under argon atmosphere.

2.2. Synchrotron powder X-ray diffraction

PXRD data were collected at the BL44B2 beamline, SPring-8, Japan, in Debye–Scherrer geometry with an image plate detector. The incident X-ray energy was calibrated every 24 h using PXRD patterns measured on a NIST CeO_2 standard sample with a = 5.411651 (6) Å, giving wavelengths of 0.49980 (2) Å and 0.49994 (1) Å for the low- and high-temperature measurements, respectively.

To obtain homogeneous particle sizes, important for measuring high-quality powder diffraction data, the powder sample was suspended in ethanol, mixed thoroughly, and left for sedimentation for five minutes. The supernatant containing only the smaller, non-sedimented particles was moved to another vial, mixed and again left to sediment for another five minutes. The supernatant was then moved to a final vial and the ethanol evaporated, leaving behind a fine powder of homogeneous particles. The powder was packed in 0.2 mm capillaries: glass for low-temperature (LT) and quartz for high-temperature (HT) measurements.

A N_2 gas flow system was used for cooling/heating the samples during measurements. A temperature calibration was conducted from 100 to 1000 K in 100 K increments by inserting a thermocouple at the sample position and recording the temperature 10 min after the system had reached its set point, to ensure complete thermal equilibration in the system and avoid any 'overshoot' effects from the PID controller. The LT setup (100–300 K) used a 0.5 mm × 3 mm collimator, while a 0.5 mm × 1 mm collimator was necessary for the HT setup (300–1000 K). Measurements were performed in 100 K increments in the interval 100–1000 K.

2.3. Rietveld refinements

Rietveld refinements were conducted using the *FullProf* program (Rodríguez-Carvajal, 1993). The background was modeled using selected points with refinable heights and the peak shape was a Thompson–Cox–Hastings pseudo-Voight function corrected for axial divergence asymmetry. An instrumental resolution function based on refined half-width parameters of the NIST CeO_2 standard was employed, and an absorption correction applied with μ_R = 1.30 calculated from the nominal stoichiometry, a wavelength of 0.5 Å, a capillary radius of 0.1 mm, and a packing fraction of 0.6 using Argonne National Laboratories (2021) X-ray absorption calculator. A range of 40× the full width at half-maximum was included for the calculation of the profile of individual Bragg reflections.

The following parameters were included in the refinements: scale factor, background points, zero-point correction, the Lorentzian half-width parameter X, and the asymmetry correction parameters *asy*1 and *asy*2 up to a limit of 40° 2θ, the unit-cell parameter, the 16*i* atomic position (x,x,x), the 24*k* atomic position (0,y,z), isotropic ADPs for all but the 6*d* guest site, which was modeled anisotropically, and finally the occu-

pancies of Au and Si on the host sites assuming full occupancy on each site. The refined values are given in Table S1 the supporting information.

Two minor impurity phases were identified from the diffraction pattern, pure Si and $CeAu_2Si_2$, and these were included in the refinement giving a combined weight fraction of roughly 15% throughout the temperature series. The origin of minute impurity peaks at 2θ = 8.001°, 9.065°, 12.109°, 13.605°, 18.261°, 10.290°, 12.970° and 26.688° could not be found.

2.4. Energy-dispersive X-ray spectroscopy

Energy-dispersive X-ray spectroscopy (EDX) data was measured on a Thermo Scientific Talos F200X S/TEM to show the presence of Ce within the clathrate structure. A powdered sample was suspended in ethanol and sonicated to ensure homogeneous dispersion of the particles. The mixture was then deposited on the S/TEM sample holder carbon grids and left for the ethanol to evaporate leaving behind an even dispersion of particles. X-ray collection was performed for approximately 20 min for each of the examined particles.

3. Results and discussion

3.1. Structural models

The host atoms are on the 6*c*, 16*i* and 24*k* Wyckoff sites, while the guest atoms are on 2*a* and 6*d* at the centers of the dodecahedral and tetrakaidecahedral cages, respectively. Different structural models were tested for the distribution of atoms among the different sites, and in all cases each atomic site was assumed to be fully occupied.

Transition metals have generally been observed to order on the 6*c* site in the host structure (Johnsen *et al.*, 2006, 2007; Baitinger *et al.*, 2020; Herrmann *et al.*, 1999) and Au was confined to this position in the initial model used here, with Si being present on all sites. From refining the relative Au/Si occupancy on 6*c*, the site was found to be preferentially occupied by Au: $occ_{Au}(6c)/occ_{Si}(6c)$ = 5.9 (1). This model resulted in negative values for the ADP at 24*k*, hinting at a lack of scattering power on this site in the model. Au was then added also to the 24*k* site and the relative Au/Si occupancy refined. This resulted in a significantly better fit and reasonable ADPs, despite the refined amount of Au on the site being only around 1%: $occ_{Au}(24k)/ occ_{Si}(24k)$ = 0.012 (1). Adding Au to the 16*i* site resulted in even lower Au occupancy than for 24*k* without improving the fit and as a result was not included in the final model.

Thus, the Au atoms are predominantly ordered on the 6*c* site, with a small degree of distribution across the 24*k* sublattice, in agreement with previous results in the literature for the BAS/BCAS system (Aydemir *et al.*, 2011; Jaussaud *et al.*, 2005; Prokofiev *et al.*, 2013). A similar pattern is seen in boron silicon clathrates where there is a minor substitution of boron on the 24*k* site, although in this system it is the 16*i* and not the 6*c* site that functions as the majority substitution site (Hübner, Jung, Koželj *et al.*, 2021; Hübner, Jung, Schmidt *et al.*, 2021; Jung *et al.*, 2021). The 6*c* site is unique to the extent that it is the only host site with no direct bonds to its symmetry equivalent positions, whereas direct 24*k*—24*k* and 16*i*—16*i* bonds are present in the framework structure. Thus, the propensity for Au to substitute on the *6c* site could indicate that Au—Au bonds are relatively unfavorable which thereby dictates how Au is incorporated into the host structure.

The preference for Au substitution of the 24*k* site over 16*i* can be rationalized from the difference in bonding geometry of the two. The 16*i* bonding geometry approaches the ideal tetrahedral angle of 109.47° [16*i*—16*i*—24*k* angle of 108.7 (1)° and 24*k*—16*i*—24*k* angle of 110.16 (8)°], whereas 24*k* shows significant deviation from this [6*c*—24*k*—24*k* angle of 124.23 (5)°, 16*i*—24*k*—24*k* angle of 106.71 (7)°, 16*i*—24*k*—16*i* angle of 106.0 (1)° and 6*c*—24*k*—16*i* angle of 105.98 (7)°]. The sp^3 hybridization of Si means that its bonding is much more compatible with the geometry of the 16*i* site, making it energetically favorable for Si to occupy this site, which conversely leads to preferential occupation of Au on the 24*k* site compared with 16*i*.

For the guest site, the low X-ray scattering contrast between Ba and Ce means that substituting one for the other does not significantly impact the refinement residuals. Consequently, refining the relative Ba/Ce occupancies on the guest sites is not a reliable way of determining the Ce content. Instead, the clathrate was assumed to be an ideal Zintl phase, such that the stoichiometry is determined from the 184 valence electron counting rule giving the refined host structure composition. It was assumed that each Ba and Ce atom contribute two and three electrons to the host structure, respectively (Ba^{2+} and Ce^{3+}), and that Au was monovalent. Thus, in order for charge balance to be satisfied, the following relation between the Ce and Au content must hold: Ce = 16 − 3 × Au.

The calculated amount of Ce was initially introduced in the small cage on the 2*a* site in accordance with Prokofiev *et al.* (Prokofiev *et al.*, 2013) as well as the simple chemical intuition that the smaller Ce^{+3} ion (1.15 Å ionic radius versus 1.49 Å for Ba^{2+}) would preferentially enter the small cage. Adding Ce to the 6*d* site and refining the relative amount in each cage resulted in only a very small fraction of Ce on 6*d* in the large cage, without any noticeable improvement in the model. Accordingly, Ce was solely confined to the 2*a* in the small cage. The refinement of the occupancies as described above was performed for the 100 K dataset and resulted in the composition $Ba_{7.74\ (9)}Ce_{0.26\ (9)}Au_{5.42\ (3)}Si_{40.58\ (3)}$. This composition was then fixed in the subsequent refinements of the data measured at other temperatures, as there was no evidence of any decomposition of the clathrate within the measured temperature range. Fig. 2 shows the refined powder diffraction pattern along with a visual representation of the refined occupancies and ADPs.

3.2. Unit-cell parameter

The unit-cell parameter is plotted as a function of temperature in Fig. 3(*a*). The thermal expansions obtained from the low-temperature and high-temperature data are very

similar (slope of the curve), but there is clearly an offset between the data [Fig. 3(*a*), inset]. The main differences between the data collected at LT and HT are the type of capillary (glass versus quartz) and size of collimator (0.5 mm × 3 mm versus 0.5 mm × 1 mm). In order to correct for this systematic deviation, the wavelength was altered slightly for the LT data such that the unit-cell parameter at 300 K matched that of the 300 K HT data (from 0.49980 Å to 0.50002 Å).

The coefficient of linear thermal expansion α, as determined from the slope, was found to be 7.30 (8) × 10^{-6} K^{-1}. This matches the value given by Falmbigl *et al.* (2010) for $Ba_8Au_5Si_{41}$, based on unit-cell parameters measured at 150 K and 300 K by Zeiringer (2010). A general trend appears from the data presented by Falmbigl *et al.* (2010) for Ba containing Si based clathrates, with α ranging 6.96–16.2 × 10^{-6} K^{-1}. Thus, clathrates substituted with heavier noble metals, such as Pt and Au, exhibit lower α, in accordance with the low value observed for the BCAS (Falmbigl *et al.*, 2010). The substitution of Ce for Au in the small cage does not seem to significantly affect the thermal expansion of the host lattice.

The unit-cell parameter observed at room temperature in the present study can be compared with values of BAS and BCAS found in literature as a function of the amount of Au in the structure, Fig. 3(*b*). For lower Au content the unit cell increases approximately linearly with the amount of Au, with a slight stabilization relative to this trend observed above five Au per formula unit. This may be related to the fact that it is around this amount where Au starts appearing on the 24*k* sublattice, while for lower Au content it appears to be ordered solely on the 6*c* site (Aydemir *et al.*, 2011).

Substitution of Ba for Ce (BCAS versus BAS) results in a significant decrease in the unit-cell parameter similar to the observation of Prokofiev *et al.* (2013). This matches the expectation that the unit-cell contracts slightly with the introduction of a smaller guest atom. The degree of unit-cell contraction observed here is significantly smaller than observed by Prokofiev *et al.* (2013) in agreement with the smaller Ce content determined here.

The BCAS unit-cell parameter determined by Kawaguchi *et al.* (2000) fits the trend observed for pure BAS. In that study the sample is assumed to be phase-pure clathrate with the nominal composition $Ba_6Ce_2Au_6Si_{40}$ from the synthesis, but impurity phases are clearly present in the PXRD data although not discussed. This nominal composition with high Ce content is very unlikely to be based on unit-cell reduction observed in BCAS here and by Prokofiev *et al.* (2013), and in these two studies the amount of Ce in the structure is significantly lower than the nominal composition. Taken together with the presence Ce-rich impurity phases, there is clear evidence that Ce incorporation in the clathrate structure is not straightforward. The similarity between the unit-cell parameter of Kawaguchi *et al.* and those of other BAS clathrates suggests that very little, if any, Ce is incorporated in their

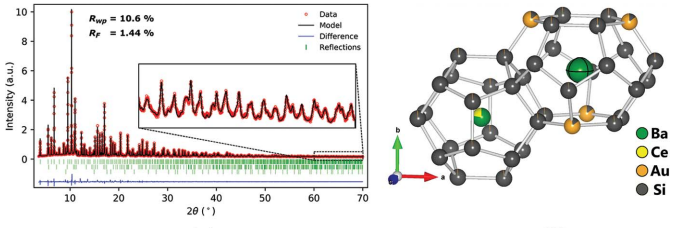

(*a*) (*b*)

Figure 2
(*a*) PXRD pattern measured at 100 K (red dots) along with the refined model (black line) and the difference plot (blue line). The indexed peaks (green bars) are given in order from the top: BCAS, $CeAu_2Si_2$ and Si. A few minute impurity phase reflections (2θ = 8.001°, 9.065°, 12.109°, 13.605°, 18.261°, 10.290°, 12.970°, 26.688°) have not yet been described. (*b*) The final refined model showing the distribution of elements on the different sites. The thermal ellipsoids are drawn at the 99% probability at 1000 K for the sake of visibility. In the anisotropic model, the 6*c* site shows a slight anisotropy with preference for vibration in the plane of the tetrakaidecahedra (parallel to the hexagonal faces).

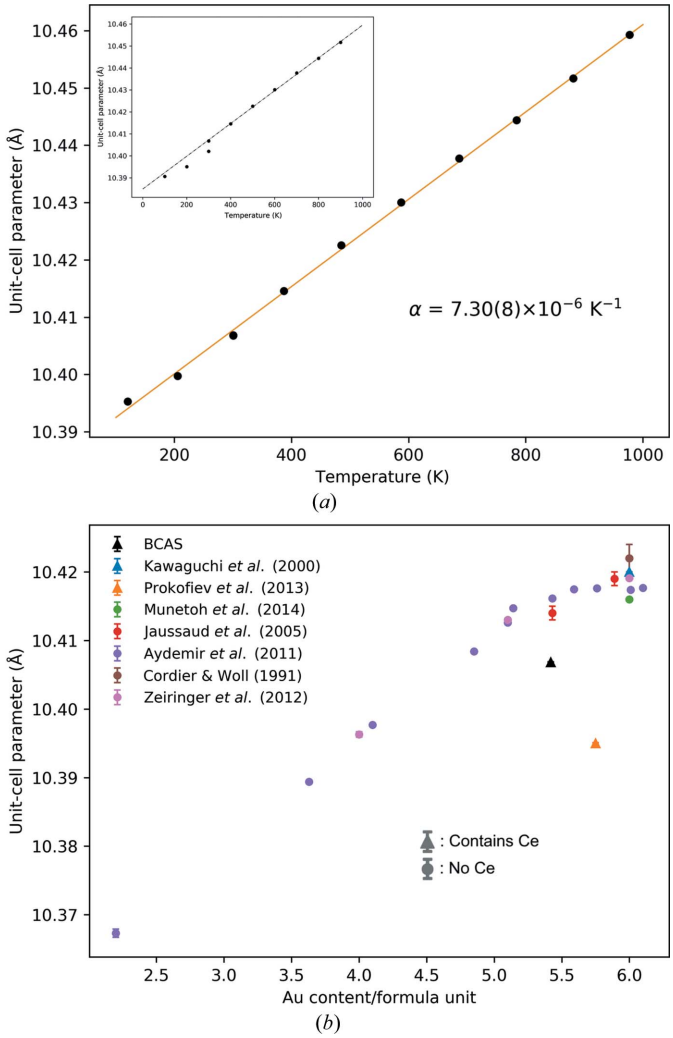

Figure 3
(*a*) Unit-cell parameter as a function of temperature along with a linear fit and the coefficient of linear thermal expansion determined from its slope; inset shows the systematic deviation between the LT and HT data before the wavelength was adjusted for the LT data. (*b*) Comparison of unit-cell parameter at room temperature for various BCAS (triangles) and BAS (circles) samples as a function of Au content.

clathrate structure. The host structure responds to the nature of the guest atom and the unit-cell parameter provides a sensitive probe for the structural composition.

A strong point of powder diffraction is the division of scattering from different crystalline phases into separate sets of (overlapping) Bragg peaks. The present Rietveld refinement also models the two impurity phases of $CeAu_2Si_2$ and Si. In the supporting information the refined parameters are listed and plotted for the impurity phases. For $CeAu_2Si_2$ the linear thermal expansion coefficients are 13.6 (2) $\times 10^{-6}$ K^{-1} and 5.1 (1) $\times 10^{-6}$ K^{-1} for the *a*-axis and *c*-axis, respectively, while it is estimated to be 2.71 (4) $\times 10^{-6}$ K^{-1} for Si.

3.3. Confirmation of Ce in the clathrate structure

The decrease in unit-cell parameter of our clathrate is only indirect evidence of the presence of Ce in the clathrate structure. Scanning transmission electron microscopy–energy-dispersive X-ray spectroscopy (STEM-EDX) was used as a secondary method of verification for the presence of Ce in the clathrate structure. Fig. 4 shows the elemental mapping of two particles, from which it is clear that all elements are dispersed evenly throughout, and that there is no agglomeration of Ce in small impurity regions.

Results of the elemental quantification from the STEM-EDX data is shown in Table 1. Comparison of the obtained values match the expected values for the refined composition reasonably well. Considering the detected Ce amounts, it appears that the quantity in the structure may be higher than the value obtained from the host composition by assuming an ideal Zintl phase. This assumption is also quite naïve, especially when looking at the wide composition range of $Ba_8Au_xSi_{46-x}$ ($3.63 \leq x \leq 6.1$) (Aydemir *et al.*, 2011), which shows that many compositions outside the ideal Zintl composition of x = 5.33 are possible for this compound. The refined wt% of BCAS was on the order of 85% which, together with the reasonable match in chemical composition from STEM-EDX, makes it very unlikely that the particles are composed of anything other than BCAS (except for the small Si protrusion highlighted for the second particle). Thus, we conclude that Ce indeed has been successfully incorporated into the clathrate structure.

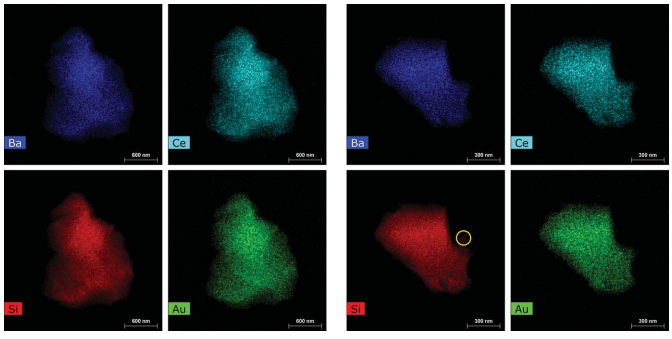

Figure 4
EDX images showing the elemental distribution of Ba (blue), Si (red), Ce (cyan) and Au (green) in two clathrate particles. The elements are dispersed evenly throughout both particles, except for a small Si protrusion on the second particle (yellow circle), showing that Ce has been incorporated into the clathrate structure.

Table 1
Relative elemental quantification of the STEM-EDX data along with the expected at.% from the refined BCAS composition for comparison.

	Ba (at.%)	Ce (at.%)	Au (at.%)	Si (at.%)
Particle 1	15 (5)	1.3 (4)	12 (4)	70.8 (5)
Particle 2	14 (4)	2.1 (6)	11 (3)	72.8 (6)
$Ba_{7.74\ (9)}Ce_{0.26\ (9)}Au_{5.42\ (3)}Si_{40.58\ (3)}$	14.3 (2)	0.48 (2)	10.03 (6)	75.15 (6)

3.4. ADP modeling

3.4.1. Host atoms. The host atoms can be described as Debye oscillators which, under the assumption of a monoatomic cubic unit cell and spherical Brillouin zone, gives the temperature dependence of the isotropic mean square displacement U_{iso} as (Willis & Pryor, 1975; Bentien *et al.*, 2005)

$$U_{iso} = \frac{3\hbar^2 T}{m k_B \Theta_D^2}\left[\frac{T}{\Theta_D}\int_0^{\Theta_D/T}\frac{x}{\exp x - 1}dx + \frac{\Theta_D}{4T}\right] + d^2.$$

Here, m is the mass of the atom, k_B Boltzmann's constant, $\hbar$ is the reduced Planck constant, d^2 is a constant added to account for any temperature-independent disorder, and Θ_D is the Debye temperature. Despite the simplicity of this model and its rather severe approximations, Θ_D is a useful materials characteristic which is related to the hardness of, and thus the speed of sound in, the material. The Debye temperature allows us to probe the effects of varying composition on the chemical bonding. Fits of the Debye model to the ADPs of the three host sublattices are shown in Fig. 5(*a*), and the average Debye temperature of the host framework is compared with various BAS compositions from Aydemir *et al.* (2011) in Table 2.

Similar to the unit-cell parameter, there is a minor discrepancy in the temperature dependence of the ADPs determined for the LT and HT data. Furthermore, a slight wavelike behavior is seen in the U_{iso} values, which is most pronounced for 24*k*, but the deviation from the linear trend is minor. Modeling of the average host U_{iso} yields a Θ_D of 404 (7) K, in approximate agreement with the value of 390 K obtained by Aydemir *et al.* (2011) for a BAS sample with the same host composition corroborating the refined host composition. The inclusion of Ce in the small cage appears to have little effect on host structure bonding as monitored in the host structure ADPs. This is in contrast to the unit-cell parameter, which show a significant effect upon Ce inclusion, Fig. 3(*b*).

There is a significant difference between the Debye temperatures for the three individual host sites, as seen in Fig. 5(*a*), where 6*c* [214 (4) K] is significantly lower than 16*i* [559 (17) K] and 24*k* [481 (13) K]. The difference is likely due to the difference in chemical species on each of the sites: 6*c* is mostly occupied by Au, 24*k* has a small fraction of Au, while 16*i* exclusively is Si. Comparing the two elements, the noble

Table 2
Debye and Einstein temperatures for BCAS along with values for different BAS composition as determined by Aydemir *et al.* (2011).

Composition	Θ_D (K)	$\Theta_{E,iso}(2a)$ (K)	$\Theta_{E,11}(6d)$ (K)	$\Theta_{E,22}(6d)$ (K)
$Ba_{7.56}Ce_{0.34}Au_{5.43}Si_{40.57}$	404 (7)	128 (2)	98 (2)	91 (2)
$Ba_8Au_{4.10}Si_{41.90}$	412† // 358‡	–	10‡	79‡
$Ba_8Au_{4.85}Si_{41.15}$	418† // 353‡	–	94‡	78‡
$Ba_8Au_{5.10}Si_{40.90}$	404†	–	–	–
$Ba_8Au_{5.14}Si_{40.86}$	407†	–	–	–
$Ba_8Au_{5.43}Si_{40.57}$	390†	–	–	–
$Ba_8Au_{5.59}Si_{40.41}$	37† // 343‡	–	84‡	76‡
$Ba_8Au_{5.76}Si_{40.24}$	362†	–	–	–
$Ba_8Au_{6.10}Si_{39.90}$	335† // 326‡	–	95‡	73‡

† From Fermi-liquid fit to C_p data. ‡ From modeling of lattice specific heat.

metal nature of Au makes its bonds significantly weaker than Si, corresponding to softer vibrations and a lower Θ_D, in agreement with the trend observed here. The relatively large difference in Θ_D for 16*i* and 24*k* supports the partial substitution of Au on the 24*k* sublattice and its absence from the 16*i* site.

The individual bond lengths in the host structure, shown in Fig. 5(*b*), mostly behave as expected with a few exceptions. The main surprising feature is the stagnation, or even slight decrease, in the 6*c*—24*k* bond length in the range from 300 K to 800 K but no explanation for this behavior has been identified yet. The great drop at 1000 K for the 24*k*–24*k* distance mirrors the deviation of the 1000 K data in other parameters, *e.g.* thermal parameters and bond lengths in Fig. 6, and is likely due to degradation of data quality as is expected for these high temperatures. The anomalous behavior of the 16*i*–16*i* distance at low temperature is reminiscent of the incongruity between the low- and high-temperature data, indicating that the effect was not entirely corrected with the change in wavelength.

3.4.2. Guest atoms. The guest atoms can be modeled as Einstein oscillators, where interactions with the framework

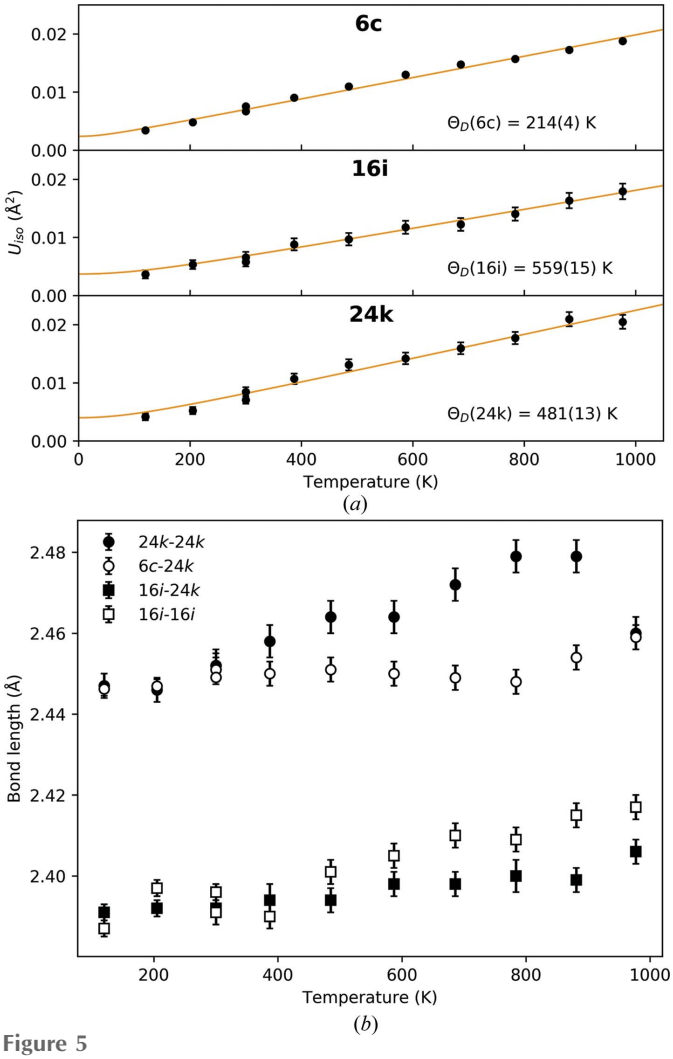

Figure 5
(*a*) The mean isotropic displacement as a function of temperature for the three host sites, along with the fitted Debye model and resulting Θ_D for each host structure site. The trend of $\Theta_D(16i) > \Theta_D(24k) > \Theta_D(6c)$ agrees with preferential occupation of 6*c* by Au and small amount on 24*k*. (*b*) The different bond lengths in the host structure as a function of temperature.

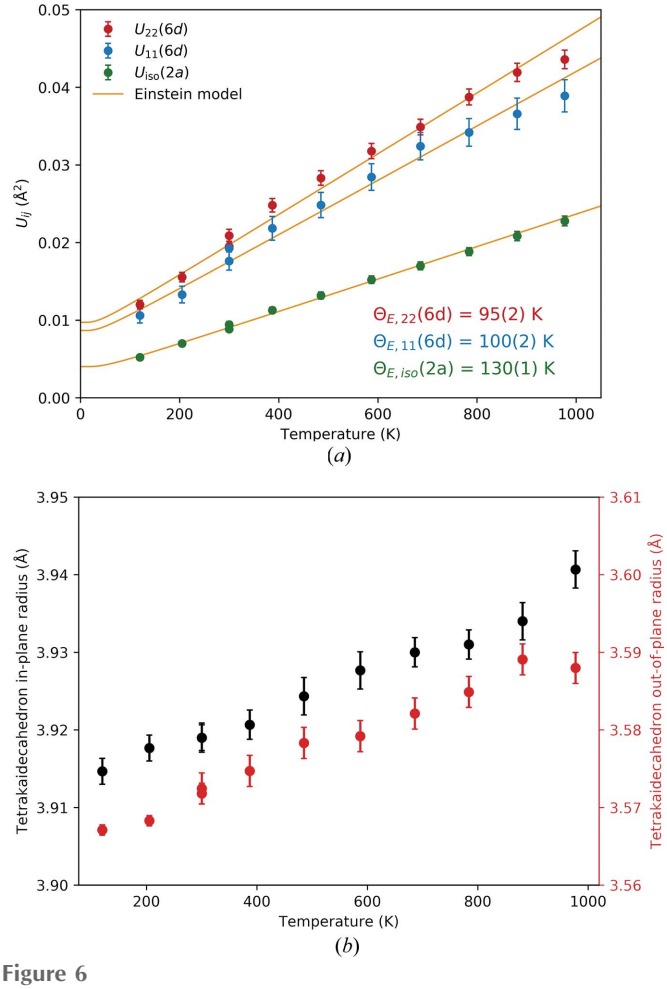

Figure 6
(*a*) The guest atom ADPs as a function of temperature along with the fitted Einstein models and corresponding Einstein temperatures. (*b*) Average distance from 6*d* to the in- and out-of-plane atoms of the large tetrakaidecahedral cage. Here the out-of-plane atoms are defined as the eight 24*k* and four 6*c* atoms that comprise the two hexagonal faces, and the in-plane atoms the four 24*k* and eight 16*i* atoms that 'zigzag' around the equatorial plane of the cage (see Figs. 2 and 7).

Table 3
Comparison of the in- and out-of-plane behavior of the 6*d* site for different clathrate compounds, as seen from the difference in anisotropic ADPs at room temperature and/or the difference in the Einstein temperatures.

The type of data used is given (PX = powder X-ray diffraction, SX = single-crystal X-ray diffraction, SN = single-crystal neutron diffraction, and C_p = specific heat). The isotropy values are calculated as the ratios U_{11}/U_{22} and $\Theta_{E,22}/\Theta_{E,11}$, such that a value of unity corresponds to perfect isotropy and lower values correspond to greater anisotropy. AM = arc melting, OFZ = optical floating zone, SnB = shake 'n bake, Br = Bridgman, Czo = Czochralski pulling, IF = induction furnace, SS = solid state.

Composition	Data type	U_{11} ($\times10^{-4}$ Å^2)	U_{22} ($\times10^{-4}$ Å^2)	$\Theta_{E,11}$ (K)	$\Theta_{E,22}$ (K)	Isotropy U_{xx}	Isotropy Θ_E	Synthesis
Rare earth clathrates								
$Ba_{7.74\ (9)}Ce_{0.26\ (9)}Au_{5.42\ (3)}Si_{40.58\ (3)}$	PX	183 (13)	205 (7)	100 (2)	95 (2)	0.89 (7)	0.95 (3)	AM
$Ba_{6.91\ (17)}Ce_{1.06\ (12)}Au_{5.75\ (25)}Si_{40.2\ (43)}$ (Prokofiev *et al.*, 2013)	SX	104 (2)	189 (1)	–	–	0.55 (1)	–	OFZ
$Eu_2Ba_6Cu_4Si_{42}$ (Mudryk *et al.*, 2002)	SX	200 (3)	331 (3)	–	–	0.60 (1)	–	SnB
$Eu_2Ba_6Al_8Si_{36}$ (Mudryk *et al.*, 2002)	SX	163 (3)	242 (2)	–	–	0.67 (1)	–	SnB
$Ba_8Au_xIVa_{46-x}$								
$Ba_8Au_{4.10}Si_{41.90}$ (Aydemir *et al.*, 2011)	C_p	–	–	101	79	–	0.78	IF
$Ba_8Au_{4.85}Si_{41.15}$ (Aydemir *et al.*, 2011)	C_p	–	–	94	78	–	0.83	IF
$Ba_8Au_{5.59}Si_{40.41}$ (Aydemir *et al.*, 2011)	C_p	–	–	84	76	–	0.90	IF
$Ba_8Au_{6.10}Si_{39.90}$ (Aydemir *et al.*, 2011)	C_p	–	–	95	73	–	0.77	IF
$Ba_8Au_{5.43}Si_{40.57}$ (Jaussaud *et al.*, 2005)	SX	163 (4)	250 (3)	–	–	0.65 (1)	–	IF
$Ba_8Au_{5.89}Si_{40.11}$ (Jaussaud *et al.*, 2005)	SX	130 (2)	204 (2)	–	–	0.64 (1)	–	IF
$Ba_8Au_6Si_{40}$ (Cordier & Woll, 1991)	SX	218 (19)	299 (13)	–	–	0.73 (7)	–	SnB
$Ba_8Au_6Ge_{40}$ (Cordier & Woll, 1991)	SX	248 (28)	438 (23)	–	–	0.56 (7)	–	SnB
$Ba_8Au_{5.3}Ge_{40.7}$ (Zhang *et al.*, 2011)	SX	182 (11)	319 (11)	–	–	0.57 (4)	–	Br
$Ba_8TM_xIVa_{46-x}$								
$Ba_8Zn_7Si_{39}$ (Nasir *et al.*, 2009)	SX	150 (1)	307 (1)	99	80	0.489 (4)	0.81	SnB
$Ba_8Ni_6Ge_{40}$ (Christensen *et al.*, 2009)	SX	221 (3)	531 (3)	85 (2)	75 (2)	0.416 (6)	0.88 (3)	SnB
$Ba_8Cu_6Ge_{40}$ (Christensen *et al.*, 2009)	SX	237 (4)	414 (4)	82 (2)	63.1 (8)	0.57 (1)	0.77 (10)	SnB
$Ba_8Zn_8Ge_{38}$ (Christensen *et al.*, 2009)	SX	191 (3)	441 (3)	84 (1)	60.0 (3)	0.433 (7)	0.71 (4)	SnB
$Ba_8Cu_{5.9}Ge_{40.1}$ (Johnsen *et al.*, 2006)	PX	182 (7)	376 (5)	92 (2)	64.3 (4)	0.48 (2)	0.70 (2)	SnB
$Ba_8Ni_6Ge_{40}$ (Johnsen *et al.*, 2007)	PX	171 (5)	463 (5)	95 (1)	79 (1)	0.37 (1)	0.83 (1)	SnB
$Ba_8Zn_{7.7}Ge_{38.3}$ (Melnychenko-Koblyuk *et al.*, 2007)	SX	202 (3)	580 (3)	85	64	0.348 (5)	0.75	SnB
$Ba_8M_xIVa_{46-x}$								
$Ba_8Al_{16}Si_{30}$ (Christensen, 2006)	SX	–	–	92 (1)	68 (1)	–	0.74 (1)	Flux
$Ba_8Al_{16}Si_{30}$ (Christensen, 2006)	SX	–	–	100 (2)	74 (1)	–	0.74 (2)	SnB
$Ba_8Al_{16}Ge_{30}$ (Christensen & Iversen, 2007)	SX	–	–	85 (1)	61 (1)	–	0.72 (1)	Czo
$Ba_8Al_{16}Ge_{30}$ (Christensen & Iversen, 2007)	SX	–	–	81 (1)	64 (1)	–	0.79 (1)	SnB
$Ba_8Al_{16}Ge_{30}$ (Christensen & Iversen, 2007)	SX	–	–	85 (1)	69 (1)	–	0.81 (1)	Flux
$Ba_8Ga_{16}Si_{30}$ (Bentien *et al.*, 2005)	PX	138 (6)	319 (4)	101	77	0.43 (2)	0.76	SS
$Ba_8Ga_{16}Si_{30}$ (Bentien *et al.*, 2005)	SN	119 (7)	339 (6)	98	69	0.35 (2)	0.70	Flux
$Ba_8Ga_{16}Ge_{30}$ (Bentien *et al.*, 2005)	PX	175 (5)	448 (4)	101	73	0.39 (1)	0.72	SS

atoms are neglected and the resulting phonon dispersion is flat. The temperature dependence of the elements of the atomic displacement tensor **U** can be described as (Bentien *et al.*, 2005)

$$U_{ij}(T) = \frac{\hbar^2}{2mk_B\Theta_{E,ij}}\coth\left(\frac{\Theta_{E,ij}}{2T}\right) + d^2,$$

where $\Theta_{E,ij}$ is the Einstein temperature of the corresponding tensor element, U_{ij}, and d^2 again is used to account for any temperature-independent disorder. 2*a* was modeled with an isotropic thermal parameter, while anisotropy was included for 6*d*, where site symmetry gives that $U_{11} \neq U_{22} = U_{33}$, with the off-diagonal elements being zero. Fig. 6(*a*) shows the ADPs as a function of temperature, along with the fitted Einstein model. The smaller cage surrounding the 2*a* site, which has partial occupancy of the slightly heavier Ce atom, has harder normal modes with smaller vibrational amplitudes as compared to the thermal vibrations of the 6*d* atoms.

The 6*d* site is occupied by Ba atoms, and in type-I clathrates the ADPs of this site typically show anisotropy with disorder and much larger displacement in the equatorial plane of the cage parallel to the hexagonal faces ($U_{22} = U_{33}$) than the out of plane motion towards the hexagonal faces (U_{11}) (Bentien *et al.*, 2005), see Table 3. The present BCAS clathrate shows a

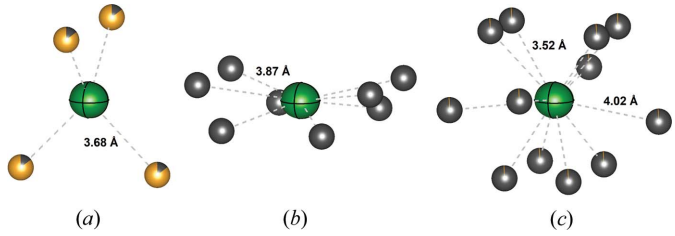

Figure 7
A closer look at the 6*d* site anisotropy and its relation to the three host sites: (*a*) 6*c*, (*b*) 16*i* and (*c*) 24*k*. Bond distances given are at room temperature.

very unusual behavior since the Ba(6*d*) atomic displacement is almost isotropic [U_{11}/U_{22} = 0.89 (7) at 300 K]. This can be due to the strong preference for Au being placed on the 6*c* site, where the presumed weaker bonding with Ba gives a relative increase in the out-of-plane motion compared with the harder interaction in the equatorial plane between Ba and Si, see Fig. 7. Such behavior has not previously been reported since the structural modeling of BAS samples in the literature used isotropic ADPs.

In BAS samples the Einstein temperatures fitted along the two directions in the large cage typically show a difference of 20–30 K, which is a relatively small anisotropy compared with values of the ADPs. When comparing Einstein temperatures for various type-I clathrates containing Ba guest atoms the isotropy (Θ_{22}/Θ_{11}) is typically around 0.7–0.8 compared with an ADP isotropy (U_{11}/U_{22}) of 0.4–0.5, as seen in Table 3. This different behavior of the isotropy of ADPs and Einstein temperatures possibly reflect their different origin. The ADPs monitor the chemical bonding environment at a specific temperature, whereas the Einstein temperatures reflect how the ADPs change with temperature. It is noteworthy that for BCAS the two Einstein temperatures are almost identical [100 (2) K and 95 (2) K] with an isotropy of 0.95 (3), comparable to the ADP isotropy.

Fig. 6(*b*) depicts the in- and out-of-plane radii of the tetrakaidecahedral cage as a function of temperature, with the radii being calculated as the mean distance to the in- (the four 24*k* and eight 16*i* atoms that do not comprise the hexagonal faces) and out-of-plane (the four 6*c* and eight 24*k* atoms comprising the hexagonal faces). The increase in these cage radii with temperature is essentially linear and with similar expansion rate, except for a deviation for the 1000 K data similar to Figs. 5 and 6(*a*). Assuming that the temperature dependence of the ADPs is governed by guest–host interaction, the approximately uniform expansion of the cage does support the similar Einstein temperatures for the in- and out-of-plane thermal vibrations.

The present Einstein temperature isotropy is unusual. Aydemir *et al.* (2011) looked at the dependence of different structural and physical properties of $Ba_8Au_xSi_{46-x}$ as a function of *x*. A transition from metallic-like to degenerate semiconductor behavior was observed around x = 5.43 as the system changes from n-type to p-type conduction, which is exceedingly close to the refined Au content found in this study. It is also around this value of *x* that the unit-cell parameter stabilizes and becomes quasi-constant, while Θ_D is quasi-constant below this value and starts to decrease as *x* increases above 5.43. $\Theta_{E,11}$ likewise shows a dependence on *x*, where it appears to reach a minimum around x = 5.43, whereas $\Theta_{E,22}$ is largely unaffected by the value of *x*. This results in a minimum in the anisotropy of the thermal motion of the 6*d* guest atom around an Au content of 5.43 per unit cell (the Zintl stoichiometry). However, it must be stressed that the isotropy of the present BCAS sample is much higher than for any of the BAS clathrates studied by Aydemir *et al.* (2011). The isotropies of U_{xx} and Θ_E for the present BCAS sample are also significantly higher than for the BCAS clathrate reported by Prokofiev *et al.* (2013) (see Table 3). They determined an Au content of x = 5.75 compared with 5.42 (3) found here, which corroborates the observation by Aydemir *et al.* (2011) of minimal anisotropy close to the Zintl stoichiometry of x = 5.43.

4. Conclusion

$Ba_{7.74\ (9)}Ce_{0.26\ (9)}Au_{5.42\ (3)}Si_{40.58\ (3)}$ clathrate was successfully grown using a two-step arc melting procedure and structural characterizations was carried out using multi-temperature high-resolution synchrotron PXRD from 100 to 1000 K. The stoichiometry was determined as based on refinement of the host structure composition and valence electron counting assuming an ideal Zintl phase. Incorporation of Ce in the structure was confirmed from with STEM-EDX along with the clear contraction in unit-cell parameter relative to pure BAS with similar Au content. From the temperature evolution of the unit-cell parameter, it was found that $\alpha = 7.30\ (8) \times 10^{-6}\ K^{-1}$, a value that matches that of pure BAS reported by Falmbigl *et al.* (2010). Accordingly, it does not appear that inclusion of Ce on the guest site affects the thermal expansion of the host structure. Au was found to mainly occupy the 6*c* site with a very minor amount on the 24*k* site and none on the 16*i* site, a trend that was corroborated from Debye modeling of the individual site ADPs where $\Theta_D(16i) > \Theta_D(24k) > \Theta_D(6c)$. Refinement of anisotropic ADPs on the 6*d* guest site showed very little difference in the in-plane ($U_{22} = U_{33}$) and out-of-plane motion (U_{11}) with U_{11}/U_{22} = 0.89 (7) which is far more isotropic than that of other type-I clathrates in literature where ratio often falls below 0.5. Einstein modeling of the temperature dependence of the guest ADPs resulted in similar isotropy of the 6*d* site, $\Theta_{E,22}/\Theta_{E,11}$ = 0.95 (3). The present Rietveld refinement also models two impurity phases of $CeAu_2Si_2$ and Si, and linear thermal expansion coefficients are for found to be 13.6 (2) $\times 10^{-6}\ K^{-1}$ and 5.1 (1) $\times 10^{-6}\ K^{-1}$ for the *a*-axis and *c*-axis of $CeAu_2Si_2$, respectively, while it is 2.71 (4) $\times 10^{-6}\ K^{-1}$ for Si.

References

Argonne National Laboratory (2021). https://11bm.xray.aps.anl.gov/absorb/absorb.php, accessed 11/10-2021.

Aydemir, U., Candolfi, C., Ormeci, A., Oztan, Y., Baitinger, M., Oeschler, N., Steglich, F. & Grin, Y. (2011). *Phys. Rev. B*, **84**, 195137.

Baitinger, M., Böhme, B., Wagner, F. R. & Schwarz, U. (2020). *Z. Anorg. Allg. Chem.* **646**, 1034–1041.

Bentien, A., Christensen, M., Bryan, J. D., Sanchez, A., Paschen, S., Steglich, F., Stucky, G. D. & Iversen, B. B. (2004). *Phys. Rev. B*, **69**, 045107.

Bentien, A., Johnsen, S. & Iversen, B. B. (2006). *Phys. Rev. B*, **73**, 094301.

Bentien, A., Nishibori, E., Paschen, S. & Iversen, B. B. (2005). *Phys. Rev. B*, **71**, 144107.

Bentien, A., Paschen, S., Pacheco, V., Grin, Y. & Steglich, F. (2003). *Proc. ICT'03.* 22nd International Conference on Thermoelectrics (IEEE Cat. No. 03TH8726), pp. 131–133. IEEE.

Candolfi, C., Aydemir, U., Baitinger, M., Oeschler, N., Steglich, F. & Grin, Y. (2012). *J. Appl. Phys.* **111**, 043706.

Christensen, M. (2006). Thesis, University of Aarhus, Department of Chemistry, Denmark.

Christensen, M., Abrahamsen, A. B., Christensen, N. B., Juranyi, F., Andersen, N. H., Lefmann, K., Andreasson, J., Bahl, C. R. & Iversen, B. B. (2008). *Nat. Mater.* **7**, 811–815.

Christensen, M. & Iversen, B. B. (2007). *Chem. Mater.* **19**, 4896–4905.

Christensen, M., Johnsen, S. & Iversen, B. B. (2010). *Dalton Trans.* **39**, 978–992.

Christensen, M., Johnsen, S., Juranyi, F. & Iversen, B. B. (2009). *J. Appl. Phys.* **105**, 073508.

Christensen, M., Juranyi, F. & Iversen, B. B. (2006). *Physica B*, **385–386**, 505–507.

Christensen, M., Lock, N., Overgaard, J. & Iversen, B. B. (2006). *J. Am. Chem. Soc.* **128**, 15657–15665.

Cohn, J., Nolas, G., Fessatidis, V., Metcalf, T. & Slack, G. (1999). *Phys. Rev. Lett.* **82**, 779–782.

Cordier, G. & Woll, P. (1991). *J. Less-Common Met.* **169**, 291–302.

Falmbigl, M., Rogl, G., Rogl, P., Kriegisch, M., Müller, H., Bauer, E., Reinecker, M. & Schranz, W. (2010). *J. Appl. Phys.* **108**, 043529.

Gatti, C., Bertini, L., Blake, N. P. & Iversen, B. B. (2003). *Chem. Eur. J.* **9**, 4556–4568.

Herrmann, R. F. W., Tanigaki, K., Kawaguchi, T., Kuroshima, S. & Zhou, O. (1999). *Phys. Rev. B*, **60**, 13245–13248.

Hübner, J.-M., Jung, W., Koželj, P., Bobnar, M., Cardoso–Gil, R., Burkhardt, U., Böhme, B., Baitinger, M., Schwarz, U. & Grin, Y. (2021). *Z. Anorg. Allg. Chem.* **647**, 119–125.

Hübner, J.-M., Jung, W., Schmidt, M., Bobnar, M., Koželj, P., Böhme, B., Baitinger, M., Etter, M., Grin, Y. & Schwarz, U. (2021). *Inorg. Chem.* **60**, 2160–2167.

Jaussaud, N., Gravereau, P., Pechev, S., Chevalier, B., Ménétrier, M., Dordor, P., Decourt, R., Goglio, G., Cros, C. & Pouchard, M. (2005). *C. R. Chim.* **8**, 39–46.

Johnsen, S., Bentien, A., Madsen, G. K. H., Iversen, B. B. & Nygren, M. (2006). *Chem. Mater.* **18**, 4633–4642.

Johnsen, S., Bentien, A., Madsen, G. K. H., Nygren, M. & Iversen, B. B. (2007). *Phys. Rev. B*, **76**, 245126.

Jung, W., Böhme, B., Hübner, J. M., Burkhardt, U., Borrmann, H., Bobnar, M., Nguyen, H. D., Pantenburg, I., Etter, M., Schwarz, U., Grin, Y. & Baitinger, M. (2021). *Dalton Trans.* **50**, 1274–1282.

Kawaguchi, T., Tanigaki, K. & Yasukawa, M. (2000). *Phys. Rev. Lett.* **85**, 3189–3192.

Melnychenko-Koblyuk, N., Grytsiv, A., Fornasari, L., Kaldarar, H., Michor, H., Röhrbacher, F., Koza, M., Royanian, E., Bauer, E., Rogl, P., Rotter, M., Schmid, H., Marabelli, F., Devishvili, A., Doerr, M. & Giester, G. (2007). *J. Phys. Condens. Matter*, **19**, 216223.

Mudryk, Y., Rogl, P., Paul, C., Berger, S., Bauer, E., Hilscher, G., Godart, C. & Noël, H. (2002). *J. Phys. Condens. Matter*, **14**, 7991–8004.

Munetoh, S., Saisho, M., Oka, T., Osada, T., Miura, H. & Furukimi, O. (2014). *J. Electron. Mater.* **43**, 2430–2434.

Nasir, N., Grytsiv, A., Melnychenko-Koblyuk, N., Rogl, P., Bauer, E., Lackner, R., Royanian, E., Giester, G. & Saccone, A. (2009). *J. Phys. Condens. Matter*, **21**, 385404.

Nesper, R. (2014). *Z. Anorg. Allg. Chem.* **640**, 2639–2648.

Nolas, G., Cohn, J., Slack, G. & Schujman, S. (1998). *Appl. Phys. Lett.* **73**, 178–180.

Osakabe, Y., Tatsumi, S., Kotsubo, Y., Iwanaga, J., Yamasoto, K., Munetoh, S., Furukimi, O. & Nakashima, K. (2018). *J. Electron. Mater.* **47**, 3273–3276.

Paschen, S., Pacheco, V., Bentien, A., Sanchez, A., Carrillo-Cabrera, W., Baenitz, M., Iversen, B., Grin, Y. & Steglich, F. (2003). *Phys. B*, **328**, 39–43.

Prokofiev, A., Sidorenko, A., Hradil, K., Ikeda, M., Svagera, R., Waas, M., Winkler, H., Neumaier, K. & Paschen, S. (2013). *Nat. Mater.* **12**, 1096–1101.

Rodríguez-Carvajal, J. (1993). *Phys. B*, **192**, 55–69.

Saisho, M., Bin, L., Nagatomo, Y., Nakakohara, Y., Teranishi, R. & Munetoh, S. (2012). *J. Phys. Conf. Ser.* **379**, 012009.

Sales, B. C., Chakoumakos, B. C., Jin, R., Thompson, J. R. & Mandrus, D. (2001). *Phys. Rev. B*, **63**, 245113.

Sales, B. C., Chakoumakos, B. C., Mandrus, D. & Sharp, J. W. (1999). *J. Solid State Chem.* **146**, 528–532.

Shevelkov, A. V. & Kovnir, K. (2010). *Zintl Phases*, *Structure and Bonding*, Vol. 139, pp. 97–142.

Slack, G. A. (1995). *CRC Handbook of Thermoelectrics*, edited by D. M. Rowe, pp. 407–440. Boca Raton, FL: CRC Press.

Takasu, Y., Hasegawa, T., Ogita, N., Udagawa, M., Avila, M. A., Suekuni, K., Ishii, I., Suzuki, T. & Takabatake, T. (2006). *Phys. Rev. B*, **74**, 174303.

Tse, J. S., Iitaka, T., Kume, T., Shimizu, H., Parlinski, K., Fukuoka, H. & Yamanaka, S. (2005). *Phys. Rev. B*, **72**, 155441.

Willis, B. T. M. & Pryor, A. W. (1975). *Thermal Vibrations in Crystallography*. Cambridge University Press.

Yamasoto, K., Osakabe, Y., Adachi, S., Munetoh, S. & Furukimi, O. (2016). *MRS Adv.* **1**, 3941–3946.

Zeiringer, I. (2010). Thesis, University of Vienna, Austria.

Zeiringer, I., Chen, M., Grytsiv, A., Bauer, E., Podloucky, R., Effenberger, H. & Rogl, P. (2012). *Acta Mater.* **60**, 2324–2336.

Zhang, H., Borrmann, H., Oeschler, N., Candolfi, C., Schnelle, W., Schmidt, M., Burkhardt, U., Baitinger, M., Zhao, J.-T. & Grin, Y. (2011). *Inorg. Chem.* **50**, 1250–1257.